ARTICLE OPEN

Check for updates

Conveyor-mode single-electron shuttling in Si/SiGe for a scalable quantum computing architecture

Inga Seidler[1], Tom Struck[1], Ran Xue[1], Niels Focke[1], Stefan Trellenkamp[2], Hendrik Bluhm[1] and Lars R. Schreiber[1]✉

Small spin-qubit registers defined by single electrons confined in Si/SiGe quantum dots operate successfully and connecting these would permit scalable quantum computation. Shuttling the qubit carrying electrons between registers is a natural choice for high-fidelity coherent links provided the overhead of control signals stays moderate. Our proof-of-principle demonstrates shuttling of a single electron by a propagating wave-potential in an electrostatically defined 420 nm long Si/SiGe quantum-channel. This conveyor-mode shuttling approach requires independent from its length only four sinusoidal control signals. We discuss the tuning of the signal parameters, detect the smoothness of the electron motion enabling the mapping of potential disorder and observe a high single-electron shuttling fidelity of 99.42 ± 0.02% including a reversal of direction. Our shuttling device can be readily embedded in industrial fabrication of Si/SiGe qubit chips and paves the way to solving the signal-fanout problem for a fully scalable semiconductor quantum-computing architecture.

npj Quantum Information (2022)8:100 ; https://doi.org/10.1038/s41534-022-00615-2

INTRODUCTION

As single electron-spin qubits confined in electrostatically defined Si/SiGe quantum dots (QDs) have overcome the fidelity threshold for quantum error correction for both single and two-qubit gates[1–6] and high-fidelity qubit readout has become accessible[7–9], the research focus has been moving towards scalable quantum computing architectures[10–15]. As dense packing of semiconductor qubit at the natural coupling range of order 100 nm would lead to a prohibitive wiring density and leave no space for additional components such as readout sensors, reservoirs or control circuits, a key enabling element for scalability is a coherent qubit coupling-mechanism over at least a few microns. Such a solution could connect dense qubit registers or enable dilute qubit arrays, in each case overcoming the signal-fanout problem, i.e., fan out the signal lines from densely packed electrostatic gates to control electronics[11]. Coupling via spin-to-photon-to-spin conversion by transferring the spin information to a cavity mode is promising for bridging even longer millimeter-scale distance[16–20]. However, the large footprint of the cavities makes it less suitable for micron scale coupling, and the prospects of achieving the required fidelities well above the error-correction threshold remain unclear.

Shuttling the electron qubit itself towards another (static) qubit is a promising approach for spin-coherent medium range coupling, since it would enable local exchange-based high-fidelity two-qubit gate and suppress any residual coupling to other distant qubits. Electron transfer and entanglement of two separately transferred spins shuttled by a surface acoustic wave has been shown for GaAs/(Al,Ga)As based devices[21–25]. In this case, the transfer velocity is constrained to the material's sound velocity, and the shuttling waves are generated globally so that also static qubits are exposed to them, which can induce uncontrolled orbital excitation. Furthermore, the implementation in Si-based platforms requires an additional proximal material with high piezoelectricity[26]. Controlling the electron shuttling by an array of metal gates is thus a natural choice and has been demonstrated[27–30]. In all these demonstrations, electrons are shuttled via a series of Landau-Zener transitions through a one-dimensional array of tunnel-coupled QDs (termed bucket-brigade mode shuttling)[31–35], the tunnel-coupling and chemical potential of which need to be carefully tuned by the applied voltages. The longer the shuttling device, the more input signals are required increasing the tuning complexity, so that the fanout problem persists[36].

Here, we overcome these limitations with a mode of single electron shuttling termed conveyor mode in a shuttling device named quantum bus (QuBus), which we realized in an undoped Si/SiGe heterostructure. Conveyor-mode shuttling is based on four input signals which form a propagating sinusoidal potential. The electron is transported smoothly and adiabatically in one of the pockets of the propagating wave[36]. In contrast to other approaches, the number of gates required for a QuBus device is thus independent from its length and effort for tuning is largely reduced, thus addressing the signal-fanout problem. The velocity, acceleration and transfer distance can be adjusted by changing the frequency and duration of the input signals. Furthermore, the fabrication of the QuBus is technologically identical to the fabrication of the electrostatically defined linear QD-arrays, the fabrication of which has been shown to be industrially feasible[37,38]. We show smooth shuttling by time-resolved tracking of the electron motion and shuttling fidelities above 99% at drive voltages well within the range typically used for quantum dot control. These results show that trapping of the shuttled electrons due to disorder, one of the most concerning potential failure modes of the QuBus device, is actually not a severe limitation in Si/SiGe.

RESULTS

Shuttling concept

Before the proof-of-principle demonstration of electron shuttling, we explain the concept of conveyor-mode shuttling in our QuBus device. The device consists of three patterned metal-gate layers

[1]JARA-FIT Institute for Quantum Information, Forschungszentrum Jülich GmbH and RWTH Aachen University, Aachen, Germany. [2]Helmholtz Nano Facility (HNF), Forschungszentrum Jülich, Jülich, Germany. ✉email: lars.schreiber@physik.rwth-aachen.de

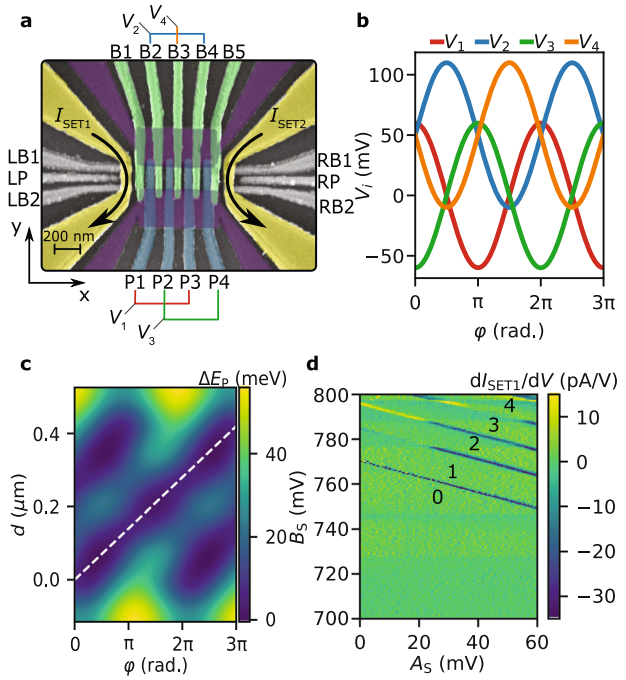

Fig. 1 Device layout and shuttling pulse. a Colored scanning electron micrograph (SEM) of the three-gate layer design used for the device. Lines indicate electrical connections among clavier gates labeled B_i and P_i. $V_i(t)$ labels the voltage signal trace applied to electrically connected gate sets. The accumulation gate of each SET is marked in yellow. **b** Voltage traces $V_i(t)$ applied to the electrically connected gate sets as indicated in panel a during electron shuttling plotted as a function of $\varphi(t)$ where we here set $A_S = 60$ mV, $B_S = 0$ V and $\Delta B_S = 50$ mV. **c** Electrostatic simulation of the potential difference ΔE_p in the strained Si quantum well underneath the clavier gates, if only the voltages $V_i(t)$ applied to the clavier gates according to **b** are taken into account. The position of the shuttled QD is indicated by a dotted white line. The simulation uses an offset ΔB_S between the gate layers of 50 mV, a shuttling amplitude A_S of 60 mV and a Voltage of −150 mV is applied to the screening gates. **d** Charge diagram where the amplitude of the shuttling pulse is varied on the *x*-axis and the total voltage offset on the channel gates is changed along the *y*-axis. The numbers in the image indicate the electron filling at that point.

fabricated on top of a planar Si/SiGe heterostructure (see Methods for details). The long screening gates in the lowest metal layer (colored purple in Fig. 1a) are kept at 0 V throughout the entire measurement and form a one-dimensional electron channel (1DEC) along the x-direction in the Si/SiGe quantum well. At each end of the 1DEC, a single electron transistor (SET) is induced by accumulation gates (colored yellow, purple in Fig. 1a), barrier gates (LB1, LB2, RB1, RB2) and plunger gates (LP and RP). The SET serves a dual purpose as proximal charge detector and electron reservoir tunnel-coupled to the 1DEC. The B and P gates on top of the 1DEC could form up to four QDs (barriers B_i, plungers P_i), but here they are used to create a traveling wave-shaped potential in the 1DEC and are referred to as the clavier gates. The same voltages are applied to each fourth gate as indicated by the labels V_1, V_2, V_3 and V_4 in Fig. 1a. The gates B_1 and B_5 are each connected separately to control the tunnel barrier between each end of the 1DEC and the SET. For shuttling, we apply a simple sine voltage to the clavier gates (Fig. 1b):

$$V_i = A_S \cos(\varphi(t) - \pi/2(i-1)) + B_S + \Delta B_S((i+1) \bmod 2) \quad (1)$$

where $i = 1 \ldots 4$ and the phase is given by $\varphi(t) = 2\pi f \cdot t$ with f and t being the shuttling frequency and shuttling time, respectively. A_S is the common amplitude of the sine waves, B_S and ΔB_S are the dc voltage offset on all the clavier gates and the additional offset used for V_2 and V_4, respectively.

This signal creates a shiftable periodic potential in the 1DEC with a smoothly propagating QD moving from the left side, at $d = 0$ nm, to the right side, at $d = 420$ nm, corresponding to a $\phi_{max} = 3\pi$, marked by the white dashed line in Fig. 1c. The pitch of the clavier gates $g = 70$ nm determines the wavelength $\lambda = 4g = 280$ nm of the potential in the 1DEC. Note that we need to apply a different voltage offset ΔB_S to compensate for the different lever arms to the 1DEC, which arise since the P- and B-gates are fabricated on the second and third metal layer, respectively. The pitch of the clavier gates is optimized for large confinement and to avoid the unintentional formation of a double dot potential (i.e., breaking apart of the moving QD) in the presence of potential disorder. This is possible by allowing for a slight breathing of the confinement potential as discussed by numeric simulations of our shuttle device[36].

To initiate electron shuttling, the 1DEC is depleted by a flush pulse sequence (see Methods) and one single electron is then loaded from an SET, tuned by B_S and A_S at $\varphi = 0$ (charge diagram in Fig. 1d for left SET), where B_S sets the overall chemical potential within the 1DEC and A_S the confinement of the QD formed at the left end of the 1DEC. For a measurement of the loading process, the tunnel barrier between SET and 1DEC is transparent (set by the voltage on gate B_1). After loading an electron, the tunnel barrier is set opaque completing the initialization of the QuBus. The charge diagram in Fig. 1d and tuning of the tunnel barriers to the reservoirs with similar charge diagrams poses the only voltage tuning required for our QuBus (see Supplementary Fig. 1 for details).

Shuttling proof-of-principle

For the proof-of-principle demonstration, we implement two shuttling pulse sequences: (I) Shuttling forth and back starting from the left hand side of the 1DEC. (II) Shuttling through the 1DEC from left to right hand side. We label the different pulse segments in the following way: S_n denotes a shuttling pulse segment moving the electron by a distance of $n\lambda$ along the x-direction. P_a and D_a are charge preparation and detection pulse segments with index a being L and R for left or right side of the QuBus, respectively. Measuring the sensor currents throughout each pulse sequence allows us to obtain single-shot time-resolved data.

For the first pulse sequence, we assemble five different pulse segments: P_L, S_1, D_L, S_{-1}, D_L (Fig. 2a). During P_L, (marked green in Fig. 2a), a single electron is loaded from the left SET, as detected by the signal step of the left SET current from 0.17 nA down to 0.09 nA, since charging the 1DECs slightly modifies the operation point of the SET's *I*–*V* characteristic. After loading the electron, the tunnel barrier to the SET is raised again to complete the initialization. During the first shuttling segment S_1 indicated in blue, the electron is moved to the right (positive *x*-direction) by a distance 1λ. To check whether the electron has moved, a detection segment D_L, colored in red, is included. The second shuttling segment S_{-1} transfers the electron back from the right to the left (negative *x*-direction) by 1λ. The second detection segment D_L determines whether the electron has returned to its initial position. The short segment marked in yellow in Fig. 2a prepares the detection and before each red region the potential of the whole 1DEC is raised to the zero electron occupation regime (cf. Fig. 1d) such that an electron confined at the left hand side of the 1DEC can tunnel through the transparent barrier to the SET. This tunneling is detected as a current step from 0.06 nA to 0.11 nA (marked in Fig. 2a). The current step height is approximately equal to the one for filling the 1DEC by one electron. The slight difference occurs as the operating point of the SETs is slightly different at loading and unloading due to

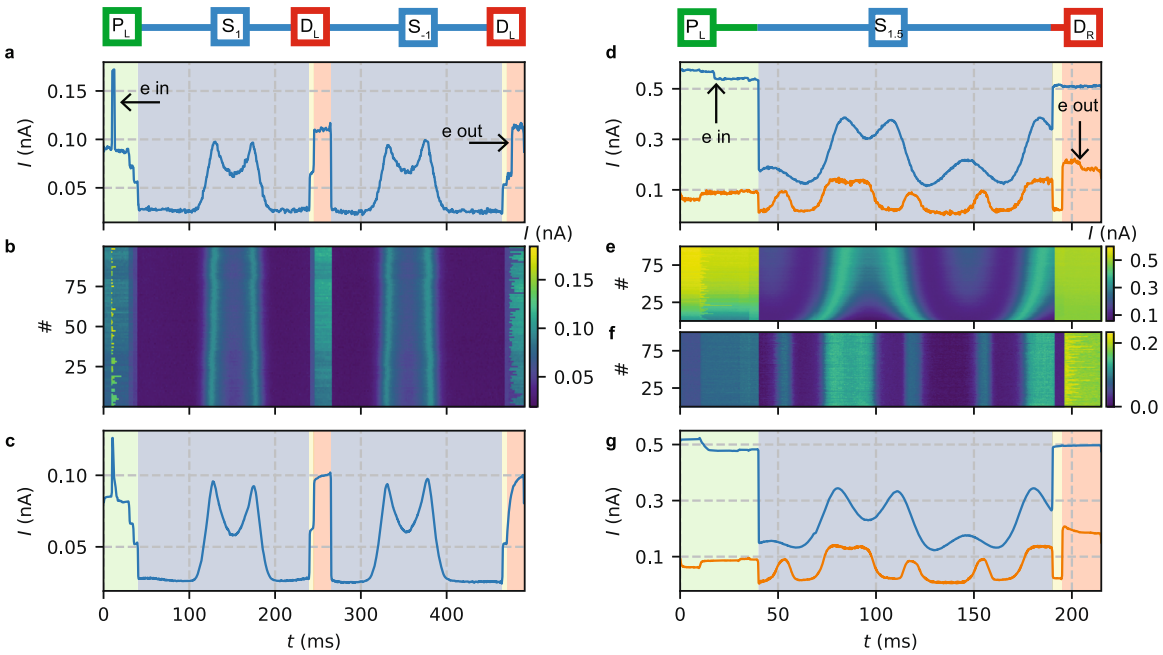

Fig. 2 Sensor signal traces for two shuttling pulse sequences. Firstly, a shuttling back and forth in the device is realized by loading an electron on the left, shuttling a distance of λ to the right, detecting on the left, shuttling a distance of λ to the left and detecting on the left (**a**–**c**). The second pulse sequence shuttling through the device consists of loading on the left, shuttling 1.5λ to the right and detecting on the right (**d**–**g**). The pulse sequences are indicated above the panels. **a** Single trace of the sensor response for shuttling in and out on the left. The plot background color marks the duration of each pulse segment. **b** Left sensor signal of 100 shuttling traces. **c** Average sensor response of the 100 shuttling traces in **b**. **d** Single trace of left (blue) and right (orange) sensor response for shuttling through the device. **e** Left sensor signal of 100 shuttling traces. The current background change is due to automatic tuning of the sensor set point. **f** Right sensor signal of the same 100 shuttling traces. **g** Average sensor response of the 100 shuttling traces depicted in **e**, **f**. Both pulse sequences are applied with $A_S = 50$ mV, $B_S = 730$ mV and $\Delta B_S = 100$ mV.

capacitive coupling to the clavier gates. Most significantly, there are no such SET current steps observed during the first D_L segment, which proves the absence of the electron in the emerged left QD and thus certifies successful shuttling. Note that all voltages applied to gates during the first and second D_L are equal, since the shuttling distance is 1λ, which implies the formation of the new QD on the left hand side of the 1DEC after S_1. This QD remains unoccupied, since no electron is detected during the first D_L, The demonstrated absence of an electron in this dot also proves that the electron does not tunnel between minima of the propagating periodic potential and that the tunnel barrier to the SET is opaque. The suppression of tunneling between different potential minima is a crucial requirement for deterministic shuttling and shows that the potential barrier is sufficiently large. Using a multiple of λ as a shuttling distance is handy for the simplicity of our proof, since the operation point of the SET is altered heavily by cross-capacities coupling of the the clavier gates to the sensor QD of the SET giving rise to the current oscillations (following the SETs Coulomb peak of its I–V characteristic) during S_1 and S_{-1}. Since we shuttled by a distance of 1λ, the sensitivity of the SET is equal during both D_L segments.

So far we discussed a single-shot trace of the shuttling sequence. Its reproducibility becomes clear from plotting 100 single shot traces recorded by looping the pulse sequence (Fig. 2b). During the preparation segment, the stochastic nature of the electron tunneling event into the 1DEC is reflected by the duration of the SET current plateau before the current step arises due to charging of the 1DEC. Similarly, the last detection segment reveals a stochastic detection of a current step in the opposite direction due to discharging of the 1DEC. In the middle, during the first detection segment, a tunneling event is clearly absent. Thus, the shuttling worked for all single-shot traces. Slight differences between traces other than the stochastic tunnel events are related to slow charge fluctuation of the QuBus device altering the operation point and sensitivity of the SET. In between single shuttling sequences, we slightly correct the operation point of the SET by the voltage applied to LB1 based on its absolute current.

When averaging over the 100 shuttling sequences from Fig. 2b, we identify the stochastic tunneling events as an exponential decrease of the sensor response and increase for P_L and the second D_L, respectively (Fig. 2c). The slight increase of current during the first detection segment is assigned to a small transient due to use of bias-tees (see method section).

Next, we prove that shuttling across the QuBus device is feasible as well. Only three pulse segments are needed: P_L, $S_{1.5}$, D_R (Fig. 2d), with P_L being identical to the previous pulse sequence. $S_{1.5}$ shifts the electron by a distance of 1.5λ, which constitutes the total length of the 1DEC. During D_R, the chemical potential of the 1DEC is raised and the tunnel barrier to the SET is set transparent by a voltage pulse applied to the B_5 gate. During P_L, a current step of the left SET indicates single electron occupation of the 1DEC on the left hand side. The current step in the right SET signal during P_L at 10 ms corresponds to a change in voltage configuration and not a tunnel event. As the the clavier gates are connected, changing to an electron loading voltage configuration is visible due to cross-capacitive coupling of the clavier gates to both SETs. During D_R, the current step of the right sensor indicates a single electron tunneling out of the 1DEC on its right hand side. (As the right SET's operation point is set to a negative flank of a Coulomb peak, the charge unload corresponds to a decrease in current here.) Repeating this pulse sequence 100 times again reveals the stochastic tunneling events in the left SET current during P_L (Fig. 2e) and in the right SET current during D_R (Fig. 2f). Conversely, no current steps are detected by the left SET during D_R and by the right SET during P_L. Thus, single shuttling events of single electrons across the 1DEC are demonstrated.

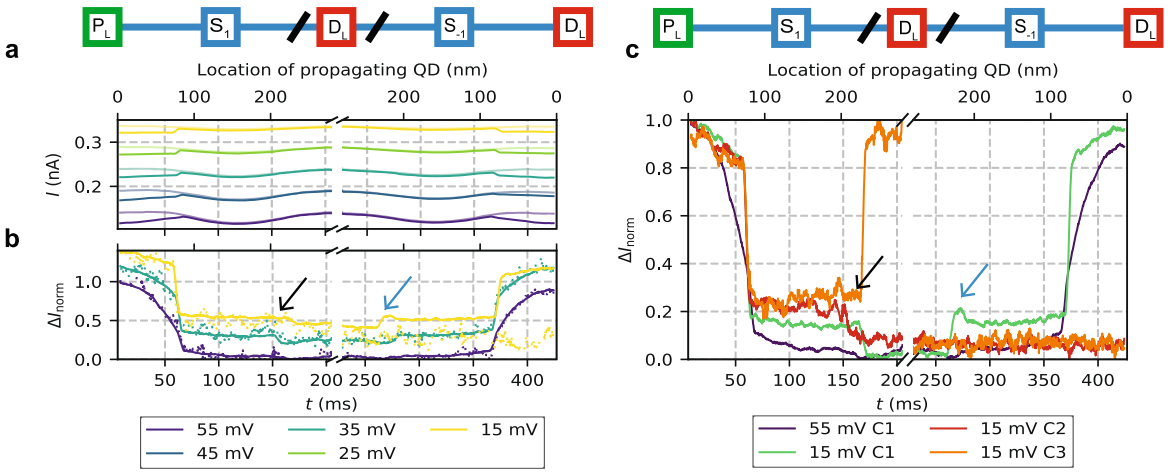

Fig. 3 Electron transfer characteristic. The pulse sequences is indicated above the panels, where the black bars mark the cut in time axis for panels below. **a** Comparison of the average shuttling signal with (dark) and without (light, reference signal) an electron loaded for different amplitude A_S values measured by the left SET compensated for cross-capacitive coupling. Shuttling signals with $B_S = 730$ mV, $\Delta B_S = 100$ mV and $f = 5$ Hz, are used. For better orientation, the upper *x*-axis indicates the minimum location of the propagating QD assuming constant shuttling velocity. The curves are offset by 0.05 nA for clarity. **b** Normalized difference of average SET currents (solid) and single traces (dotted) with one and without an electron loaded (from **a**) for different amplitude A_S. The curves are offset by 0.1 for clarity. **c** For $A_S = 15$ mV, 100 traces are bundled into three different categories: the intended transfer (C1) and two different failure modes, with $\Delta I_{norm} = 0$ during S_{-1}, if the electron is not detected by any D_L (C2) or the electron is detected during the first D_L segment (C3). Each bundle is averaged and normalized separately. The black and blue arrows in **b** highlight abrupt changes in ΔI_{norm}.

Averaging over the 100 measurement traces (Fig. 2g) reveals the expected exponential decays of the current measured by the left SET for the P_L and for the right SET for the D_R segment.

Detection during shuttling

So far, we have demonstrate that a single electron can be shuttled to each end of the 1DEC. For future spin coherent shuttling, it is desirable to avoid orbital excitations during shuttling, which might lead to spin dephasing due to state-dependent spin dynamics. Such excitations could occur if electrons tunnel from one disorder-induced potential minimum into another, rather than being transferred adiabatically in the shuttling potential. We thus investigate whether the proximal charge detectors can provide information of the smoothness of electron shuttling across the 1DEC. This smooth translation is a characteristic of our conveyor-mode approach and distinguishes it from an electron tunneling across a QD array (bucket-brigade mode)[27–29]. The capacitive cross-coupling of the clavier gates to the sensor QDs of the SET complicates direct observation of the electron movement by an SET. The signals V_i required for shuttling drastically modifies the SET's operation point and diminish its sensitivity. Thus, we compensate for the alteration of the operation point by adjusting the voltages applied to LB1 and RB1 gates during shuttling assuming a linear cross-capacity matrix (virtual gate approach[39]). This first measure keeps the sensitivity of the SET within reasonable bounds, but does not guarantee constant sensor background output during shuttling in the absence of an electron. Therefore, we interleave the looping of the shuttling pulse sequences (P_L, S_1, D_L, S_{-1}, D_L) with a nearly identical sequence providing a reference SET trace (Fig. 3a). For this reference, only the P_L segment is modified, such that no electron is loaded. All current variations in the reference trace are thus due to uncompensated capacitive cross-coupling. In Fig. 3a, we focus on the current signal during the two shuttling segments (forth and back, cf. Fig. 2a) for various amplitudes A_S (for shuttling through the device see Supplementary Fig. 2). Comparing averages of 100 single-shot shuttling traces to their corresponding (zero-electron) reference trace, we see that the detection signal of the electron shuttling approaches the one of the reference and merges at $t \approx 70$ ms, which indicates the electron moving away from the SET. When the electron returns during S_{-1}, both traces diverge again. Thus, we detect the decline of the Coulomb interaction between the single electron and the left SET during the shuttling process.

To extract more details from these averaged signal traces, we subtract each reference trace I_0 from the electron detection trace I_1 and normalize $\Delta I_{norm} = [\Delta I - \min(\Delta I)]/[\max(\Delta I) - \min(\Delta I)]$, where $\Delta I = I_0 - I_1$ (Fig. 3b). Strikingly, the averaged curves matches well a randomly picked single trace (dots in Fig. 3b) for for $A_S = (35, 55)$ mV. We conclude that the smoothness of the averaged ΔI_{norm} curve is thus not only a result of averaging stochastic tunneling events during shuttling, but each single shuttling process itself is a smooth motion as expected for the movement of the QD in the propagating potential. For the smallest amplitude $A_S = 15$ mV, a ripple appears at times marked by arrows and the initial decline is more abrupt. The averaged ΔI_{norm} at $A_S = 15$ mV does not fully recover after S_{-1}. This asymmetry is caused by the electron not returning in every single-shot trace and therefore reducing the average. Therefore, the amplitude $A_S = 15$ mV is not sufficient to confine the electron during the shuttled motion. A threshold for A_S is also expected as the confinement of moving QD has to be larger than the potential disorder due to charged defects in the device.

As we record current traces of single shuttling events, we are able to analyze individual failure modes of the electron shuttling at this small amplitude $A_S = 15$ mV. We find two typical failures within the 100 shuttling traces. We bundle these traces into three categories (C1, C2, C3) and separately average them (Fig. 3c). C1 labels shuttling forth and back without failure as confirmed by the D_L segments. For 14% of traces, labeled C2, the electrons shuttles forth, but does not return during S_{-1} and presumably get trapped in the 1DEC. (In some rare cases such electrons become unloaded during the reference shuttling sequence, prior to resetting 1DEC charge state of the flush pulse sequence described in Methods). For 5% of traces labeled C3, the shuttling failed already during S_1, at $t \approx 160$ ms (black arrow), since the detection signal suggest the electron tunnels back to the left end of the 1DEC. Also during S_{-1} at $t \approx 270$ ms (blue arrow), the traces labeled C1 show a ripple indicating a tunnel event. Note that the two arrows mark in fact the same position in the 1DEC, assuming the shuttling velocity is constant. Presumably, potential disorder in the 1DEC poses an

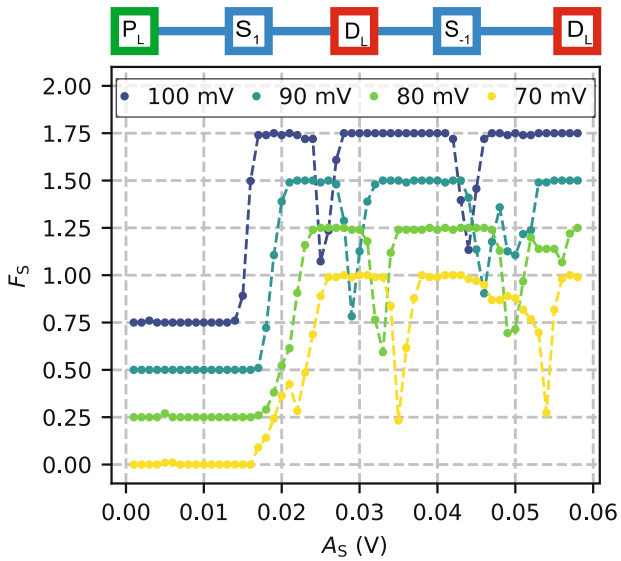

Fig. 4 Shuttle fidelity. The pulse sequence is depicted above the panel. The shuttle fidelity as a function of shuttling amplitude for different voltage offsets ΔB_S between the two different gate layers (P and B gates) with fixed $f = 1$ kHz and $B_S = 730$ mV. The electron is loaded on the left, shuttled to the right by a distance of λ, a detection segment is applied, the electron is shuttled back to the left and a second detection segment is applied. We capture the success probability P as a function of the shuttling amplitude A_S and different offsets between the gate layers ΔB_S. The shuttling sequence is counted as successful if the first D_L detects no electron and the second one does detect an electron. The curves are offset by 0.25 for clarity and solid lines are guides-to-the eye.

unintentional barrier there. For $A_S = 55$ mV, all 100 single-shot shuttling traces show no failure (C1) and abrupt steps in current are absent confirming smooth shuttling. The decline of ΔI_{norm} lasts till $t \approx 170$ ms corresponding to a shuttling distance of 230 nm and remains continuous underlining the smoothness of the electron transfer. We conclude that the intentional propagating potential in the 1DEC provides enough confinement at $A_S = 55$ mV exceeding the potential disorder. Similarly, at $t \approx 67$ ms and correspondingly at $t \approx 366$ ms the detection curves show increasing smoothness as A_S is increased (Fig. 3b, c). This analysis demonstrates that the single-electron shuttling also provides a method for mapping of electrostatic disorder.

Shuttling fidelity

We complete the failure mode analysis by measuring the shuttling fidelity F_S as a function of the amplitude A_S and offset ΔB_S of the V_i signals. This analysis confirms that A_S higher than a certain threshold allows for single electron shuttling with high F_S for the shuttling scheme (P_L, S_1, D_L, S_{-1}, D_L) looped 100 times (Fig. 4). We define a shuttling attempt as successful, if zero electron detection during the first D_L coincides with one electron detection during the second D_L segment within one shuttling trace. Here, we apply a charge detection scheme with a detection infidelity of $2 \cdot 10^{-5}$ (see Methods). F_S extracted from 100 measurement repetitions exhibits two distinct features: (I) When increasing the shuttling sine wave amplitude A_S, the first shuttling events are observed starting at approximately $A_S = 14$ mV. Once A_S is sufficiently large, the shuttling fidelity F_S mostly remains beyond 99%. This is understandable, since the expected potential disorder within the 1DEC due to charged defect has to be small compared to shuttling potential. Thus, we confirm that larger A_S and thus stronger electron confinement by the propagating wave supports smooth single electron shuttling. It also matches our observation of several failure modes at $A_S = 15$ mV (cf. Fig. 3c). (II) The F_S drops significantly for some amplitudes. These dips in F_S alter systematically with an increase in the offset ΔB_S. The characteristic dependence of the F_S dip as a function of (A_S, ΔB_S) suggest a resonance with a charge defect trapping the electron (see Supplementary Fig. 3 for details). By choosing appropriate (A_S, ΔB_S), the operation of the QuBus is ensured. We find that thermal cycling the QuBus alters and can even remove these dips entirely. We observe that shuttling the electron back and forth up to 5000 times before charge detection readout does not decrease F_S below a 100% success rate over 100 repetitions. A separate measurement at $A_S = 50$ mV, $\Delta B_S = 100$ mV, and $f = 1$ kHz indicated a fidelity $F_S = 99.42 \pm 0.02\%$ using 150,000 individual electron shuttling sequences. Note this F_S includes infidelity of the segment P_L, which we have not measured separately.

DISCUSSION

Our proof-of-principle demonstrates that conveyor-mode shuttling of a single electron in an electrostatically defined quantum channel in Si/SiGe is feasible. The four input signals V_i controlling the traveling potential are parameterized by A_S, B_S, ΔB_S, $\varphi(t)$ and can be simply tuned. Besides setting roughly the chemical potential of the quantum channel by B_S, ΔB_S, most importantly, the amplitude A_S has to be sufficiently large to confine the electron despite unintentional potential fluctuations distributed along the quantum channel. For our device, a moderate amplitude is sufficient to shuttle across the 420 nm long channel with fidelity exceeding 99%. The phase $\varphi(t)$ sets the electron shuttling velocity and de/acceleration, including the demonstrated reversal of the shuttling direction. The time-resolved comparison of a shuttling pulse sequence with none and a single electron indicates a smooth electron motion expected for the conveyor-mode. By continuous monitoring of single shuttling events, failure modes can be categorized, which provides means to localize critical potential disorder. The smoothness of the electron motion will be an important parameter for modeling spin-coherent shuttling of a spin qubit. Specifically, we expect the shuttling distance, velocity and acceleration has to balance orbital adiabaticity on the one hand and the spin dephasing and relaxation time of a static quantum dot on the other hand[40–43]. An extension of the QuBus length is possible without additional input signals. Disorder modeling and limitations for coherent electron-spin transfer are nontrivial, but promise high fidelity operation for a transfer speed of ~10 m s^{-1}, including modeling of orbital and valley excitations and variations[36]. A QuBus length of 1 to 10 micron gains sufficient space between qubit sites or dense qubit registers to interleave signal vias and control electronics tiles. For the latter, the simple control signals required for our QuBus do not need local memory on the control electronic tiles and thus ease the integration of the QuBus into a scalable quantum computing architecture. Overall, the QuBus addresses the question of medium-scale qubit connectivity for spin qubits, which is arguably the only remaining fundamental challenge regarding the scalability of this platform. It has thus the potential to become a key enabling factor to leverage the potential of semiconductor for scaling to very large systems and may make the difference between a useless and a most favorable platform for universal quantum computing.

METHODS

Setup and measurement procedures

All experiments are executed in a dilution refrigerator with a base temperature of 40 mK. All dc lines to the device are filtered by pi-filters ($f_c = 5$ MHz) at room temperature and by 2nd order RC filters with $f_c = 10$ kHz at base temperature. The clavier gates B3, P4 and B5 are connected to resistive bias-tees with a cutoff frequency of 5 Hz. Signals are applied to the ac and dc input terminal of the bias-tee, in order to effectively neutralize the bias-tees, since low-bandwidth pulses are

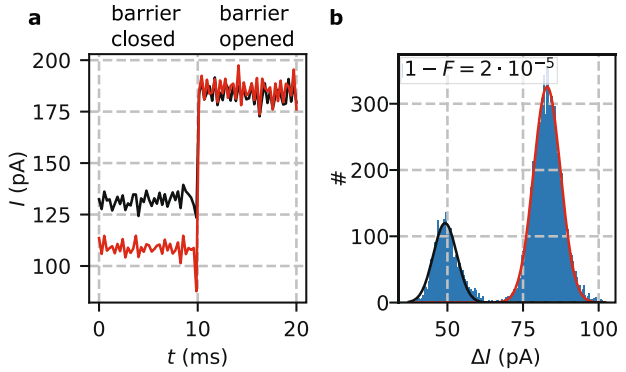

Fig. 5 Fidelity *F* of single-shot charge-readout at the ends of the shuttle device. a SET current trace *I* during the two stages of the detection segment with an electron present (red) and without an electron (black) at the end of the one-dimensional QuBus channel. During the first 10 ms, the tunnel barrier between the 1DEC and the SET is fully opaque and then fully transparent during the second 10 ms allowing an electron potentially present to immediately leave the 1DEC. **b** Histogram of the current steps Δ*I* between the two detection stages in **a** for 11,300 traces with arbitrary charge state 0 or 1 at the end of the channel before the start of the detection segment. The events covered by the two fitted Gaussians are assigned to the electron occupation 0 and 1 (red and black Gaussian fit), respectively.

sufficient for the presented experiments. A serial resistor is added to the low-frequency terminal, the value of which is tuned by flattening the sensor signal response. Electrical connections among clavier gates (Fig. 1a) are wired up outside the cryostat for flexibility reasons. Similarly, the low bandwidth wiring was chosen for practical reasons and can be replaced with high frequency lines for faster shuttling. The SETs are dc-biased by 500 µV and readout by a transimpedance amplifier and an analog-digital-converter. The data discussed were obtained after a thermal cycle to 100 K due to a blockade in the cryostat circulation. Previously, a similar behavior of the sample including electron shuttling was observed. Only the values of the dc voltages needed to be retuned.

Flush pulse sequence

To ensure an electron-free 1DEC, we apply a flush pulse-sequence to the gates before looping shuttling pulse sequences. The voltages applied to all clavier gates (B_i and P_i) are altered by 100 mV in the following sequence: first we decrease the voltage applied to gate B_3, then the one applied to P_2 and P_3, followed by a decrease on B_2 and B_4, and next on P_1 and P_4. The flush pulse segment is finished by increasing the voltages applied to gates B_1 and B_5 by 100 mV and finally resetting to the original voltages applied to the gates in reverse order. These flush pulse-sequences are particularly important for exploring failure-modes as we expect electrons to be left behind for low amplitudes. We expect these to be omitted in the high fidelity regime envisioned for quantum computing. An electron-free 1DEC can then be ensured by multiple repetitions of shuttling with larger amplitudes. The data in Figs. 3 and 4 was taken by concatenating the pulse sequences for different amplitudes. To ensure that the 1DEC remains electron free throughout the measurement, additional shuttling pulses, shuttling potentially left-behind electrons out of the 1DEC (S_{-1}+D_L), are added in between the pulse sequences for different amplitudes.

Single-shot charge detection

There are two methods applied for the detection segment D_x using the proximal SETs on either the left or the right end of the QuBus device: (I) The tunnel rate between reservoir and first QD of the 1DEC is raised to a value comparable to half the duration of the detection segment, which is long compared to the SET bandwidth. Thus, a single electron tunneling event from the first QD of the one dimensional channel can be resolved by a step in the current across the SET, as the absence of the electron alters the operating point of the SET. This method is applied for the measurements presented in Fig. 2. (II) The second charge detection method employs a two-stage SET current-readout each 10 ms long. During the first stage, the tunnel barrier between the 1DEC and the SET is opaque and then made fully transparent by pulsing the voltage applied to the barrier gate during the second stage, i.e., the tunnel rate is faster than the measurement bandwidth of 1 kHz. This results in a difference between the SET current levels measured during the two stages, which depends on the electron occupation of the QD at the end of the 1DEC before the detection segment (Fig. 5a). In the absence of the electron, this current step is determined by the cross-coupling of the barrier gate to the SET's QD alone. Plotting the observed current steps Δ*I* for 10,000 detection segments, we observe a distribution fitted by two Gaussians (Fig. 5b) assigned to the two distinct readout results. Calculated from the overlap of the two Gaussian's, the detection infidelity is $1 - F = 2 \cdot 10^{-5}$. This second method is applied for the measurements presented in Figs. 3 and 4.

Device fabrication

Figure 1a depicts the SEM inspection of a device that is fabricated identically to the measured one. It is fabricated on an undoped strained Si/SiGe heterostructure utilizing the metal lift-off technique. A 10 nm thick strained Si layer acts as the quantum well covered by a 30 nm undoped $Si_{0.7}Ge_{0.3}$ spacer and a 2 nm Si cap layer. Ohmic contacts to the quantum well layer are selectively implanted by phosphorus ions and activated by rapid thermal processing at 700 °C for 15 s. A combination of electron beam lithography, metal evaporation, metal lift-off process, and atomic layer deposition of dielectrics enables the overlay of three layers of electrically isolated metallic gates (titanium and platinum), which are insulated by 10 nm Al_2O_3 from the substrate and from each other. Each layer of metal gates consists of 5 nm Ti as the adhesion metal and a varied thickness of Pt: 15 nm, 22 nm, and 29 nm for layer 1 to layer 3 correspondingly, which robustly ensures the continuity of metal gates in a three layers stack despite the existence of an inhomogeneous local topography. The two gates colored in purple in Fig. 1a are geometrically separated by 200 nm providing a 1DEC for single electron shuttling. In this experiment, a device with 60 nm clavier gate width is measured. The clavier gates are separated by 10 nm, thus the gate pitch is $g = 70$ nm. The SETs employed as charge sensors or as electron reservoirs are formed by gates distributed among two gate layers. The charge carriers in the transport channel are accumulated by a top-gate (yellow gates in Fig. 1a.) with barrier gates (LB1, LB2, RB1, RB2) lying underneath. The sensor dots can be formed at both ends of the 1DEC symmetrically.

DATA AVAILABILITY

The datasets generated during and/or analyzed during the current study are available from the corresponding author on reasonable request.

Received: 3 April 2022; Accepted: 5 August 2022;
Published online: 30 August 2022

REFERENCES

1. Yoneda, J. et al. A quantum-dot spin qubit with coherence limited by charge noise and fidelity higher than 99.9%. *Nat. Nanotechnol.* **13**, 102–106 (2018).
2. Zajac, D. M. et al. Resonantly driven CNOT gate for electron spins. *Science* **359**, 439–442 (2018).
3. Watson, T. F. et al. A programmable two-qubit quantum processor in silicon. *Nature* **555**, 633–637 (2018).
4. Xue, X. et al. Benchmarking gate fidelities in a Si/SiGe two-qubit device. *Phys. Rev. X* **9**, 021011 (2019).
5. Xue, X. et al. Quantum logic with spin qubits crossing the surface code threshold. *Nature* **601**, 343–347 (2022).
6. Noiri, A. et al. Fast universal quantum gate above the fault-tolerance threshold in silicon. *Nature* **601**, 338–342 (2022).
7. Connors, E. J., Nelson, J. & Nichol, J. M. Rapid high-fidelity spin-state readout in Si/Si-Ge quantum dots via rf reflectometry. *Phys. Rev. Appl.* **13**, 024019 (2020).
8. Noiri, A. et al. Radio-frequency-detected fast charge sensing in undoped silicon quantum dots. *Nano Lett.* **20**, 947–952 (2020).
9. Kammerloher, E. et al. Sensing dot with high output swing for scalable baseband readout of spin qubits. Preprint at https://arxiv.org/abs/2107.13598 (2021).
10. Hollenberg, L. C. L., Greentree, A. D., Fowler, A. G. & Wellard, C. J. Two-dimensional architectures for donor-based quantum computing. *Phys. Rev. B* **74**, 045311 (2006).
11. Vandersypen, L. M. K. et al. Interfacing spin qubits in quantum dots and donors—hot, dense, and coherent. *npj Quantum Inf.* **3**, 34 (2017).

12. Veldhorst, M., Eenink, H. G. J., Yang, C. H. & Dzurak, A. S. Silicon CMOS architecture for a spin-based quantum computer. *Nat. Commun.* **8**, 1766 (2017).
13. Li, R. et al. A crossbar network for silicon quantum dot qubits. *Sci. Adv.* **4**, eaar3960 (2018).
14. Boter, J. M. et al. A sparse spin qubit array with integrated control electronics. In *Proc. IEEE International Electron Devices Meeting (IEDM)*, 31.4.1–31.4.4 (2019).
15. Boter, J. M. et al. Spiderweb Array: A Sparse Spin-Qubit Array. *Phys. Rev. Appl.* **18**, 024053 (2022).
16. Mi, X. et al. A coherent spin-photon interface in silicon. *Nature* **555**, 599–603 (2018).
17. Samkharadze, N. et al. Strong spin-photon coupling in silicon. *Science* **359**, 1123–1127 (2018).
18. Landig, A. J. et al. Coherent spin-photon coupling using a resonant exchange qubit. *Nature* **560**, 179–184 (2018).
19. Borjans, F., Croot, X., Mi, X., Gullans, M. & Petta, J. Resonant microwave-mediated interactions between distant electron spins. *Nature* **577**, 195–198 (2020).
20. Borjans, F. et al. Split-gate cavity coupler for silicon circuit quantum electrodynamics. *Appl. Phys. Lett.* **116**, 234001 (2020).
21. Hermelin, S. et al. Electrons surfing on a sound wave as a platform for quantum optics with flying electrons. *Nature* **477**, 435–438 (2011).
22. McNeil, R. P. G. et al. On-demand single-electron transfer between distant quantum dots. *Nature* **477**, 439–442 (2011).
23. Takada, S. et al. Sound-driven single-electron transfer in a circuit of coupled quantum rails. *Nat. Commun.* **10**, 4557 (2019).
24. Jadot, B. et al. Distant spin entanglement via fast and coherent electron shuttling. *Nat. Nanotechnol.* **16**, 570–575 (2021).
25. Bertrand, B. et al. Fast spin information transfer between distant quantum dots using individual electrons. *Nat. Nanotechnol.* **11**, 672–676 (2016).
26. Du, X. Y. et al. ZnO film for application in surface acoustic wave device. *J. Phys. Conf. Ser.* **76**, 012035 (2007).
27. Baart, T. A. et al. Single-spin CCD. *Nat. Nanotechnol.* **11**, 330–334 (2016).
28. Flentje, H. et al. Coherent long-distance displacement of individual electron spins. *Nat. Commun.* **8**, 501 (2017).
29. Mills, A. et al. Shuttling a single charge across a one-dimensional array of silicon quantum dots. *Nat. Commun.* **10**, 1063 (2019).
30. Yoneda, J. et al. Coherent spin qubit transport in silicon. *Nat. Commun.* **12**, 4114 (2021).
31. Zhao, X. & Hu, X. Coherent electron transport in silicon quantum dots. Preprint at https://arxiv.org/abs/1803.00749 (2019).
32. Buonacorsi, B., Shaw, B. & Baugh, J. Simulated coherent electron shuttling in silicon quantum dots. *Phys. Rev. B* **102**, 125406 (2020).
33. Krzywda, J. A. & Cywiński, L. Adiabatic electron charge transfer between two quantum dots in presence of 1/*f* noise. *Phys. Rev. B* **101**, 035303 (2020).
34. Ginzel, F., Mills, A. R., Petta, J. R. & Burkard, G. Spin shuttling in a silicon double quantum dot. *Phys. Rev. B* **102**, 195418 (2020).
35. Krzywda, J. A. & Łukasz, Cywiński Interplay of charge noise and coupling to phonons in adiabatic electron transfer between quantum dots. *Phys. Rev. B* **104**, 075439 (2021).
36. Langrock, V. et al. Blueprint of a scalable spin qubit shuttle device for coherent mid-range qubit transfer in disordered Si/SiGe/SiO_2. Preprint at https://arxiv.org/abs/2202.11793 (2022).
37. Zwerver, A. M. J. et al. Qubits made by advanced semiconductor manufacturing. *Nat. Electron.* **5**, 184–190 (2022).
38. Hutin, L. et al. All-electrical control of a hybrid electron spin/valley quantum bit in SOI CMOS technology. In *Proc. IEEE Symposium on VLSI Technology*, 125–126 (2018).
39. Nowack, K. C. et al. Single-shot correlations and two-qubit gate of solid-state spins. *Science* **333**, 1269–1272 (2011).
40. Huang, P. & Hu, X. Spin qubit relaxation in a moving quantum dot. *Phys. Rev. B* **88**, 075301 (2013).
41. Zhao, X., Huang, P. & Hu, X. Doppler effect induced spin relaxation boom. *Sci. Rep.* **6**, 23169 (2016).
42. Hollmann, A. et al. Large, tunable valley splitting and single-spin relaxation mechanisms in a Si/Si_xGe_{1-x} quantum dot. *Phys. Rev. Appl.* **13**, 034068 (2020).
43. Struck, T. et al. Low-frequency spin qubit energy splitting noise in highly purified 28 Si/SiGe. *npj Quantum Infor.* **6**, 1–7 (2020).
44. Albrecht, W., Moers, J. & Hermanns, B. HNF—Helmholtz Nano Facility. *JLSRF* **3**, A112 (2017).

ACKNOWLEDGEMENTS

The authors thank Jürgen Moers, Lieven Vandersypen and Anne-Marije Zwerver for useful discussion. This work has been funded by the German Research Foundation (DFG) under Germany's Excellence Strategy - Cluster of Excellence Matter and Light for Quantum Computing" (ML4Q) EXC 2004/1-390534769 and by the Federal Ministry of Education and Research under Contract No. FKZ: 13N14778. Project Si-QuBus received funding from the QuantERA ERA-NET Cofund in Quantum Technologies implemented within the European Union's Horizon 2020 Program. The device fabrication has been done at HNF - Helmholtz Nano Facility, Research Center Juelich GmbH[44].

AUTHOR CONTRIBUTIONS

I.S. and T.S. did the shuttling measurements and the data analysis supported by R.X. and L.R.S., I.S. and R.X. fabricated and pre-characterized the device. S.T. did electron-beam lithography. N.F. carried out electrostatic simulations for device design. L.R.S. conceived and supervised the study supported by H.B. and all authors discussed the results. T.S., I.S., R.X., and L.R.S. wrote the manuscript, which all other authors reviewed.

FUNDING

Open Access funding enabled and organized by Projekt DEAL.

COMPETING INTERESTS

I.S., H.B. and L.R.S. are co-inventors of patent applications that cover conveyor-mode shuttling and its applications.

ADDITIONAL INFORMATION

Supplementary information The online version contains supplementary material available at https://doi.org/10.1038/s41534-022-00615-2.

Correspondence and requests for materials should be addressed to Lars R. Schreiber.

Reprints and permission information is available at http://www.nature.com/reprints

Publisher's note Springer Nature remains neutral with regard to jurisdictional claims in published maps and institutional affiliations.